Preprint typeset using LaTeX style emulateapj v. 26/01/00

TWO YEARS OF INTEGRAL MONITORING OF GRS 1915+105 PART 1: MULTIWAVELENGTH COVERAGE WITH INTEGRAL, RXTE, AND THE RYLE RADIO TELESCOPE

J. Rodriguez[1], D.C. Hannikainen[2], S.E. Shaw[3], G. Pooley[4], S. Corbel[1], M. Tagger[5], I.F. Mirabel[6], T. Belloni[7], C. Cabanac[3], M. Cadolle Bel[8], J. Chenevez[9], P. Kretschmar[8], H.J. Lehto[10], A. Paizis[11], P. Varnière[12], O. Vilhu[2]

Draft version December 3, 2007

ABSTRACT

We report the results of monitoring observations of the Galactic microquasar GRS 1915+105 performed simultaneously with *INTEGRAL* and *RXTE* from 3 up to ∼300 keV, and the Ryle Telescope at 15 GHz. We present the results of the whole *INTEGRAL* campaign, report the sources that are detected and their fluxes and identify the classes of variability in which GRS 1915+105 is found. The long and continuous *INTEGRAL* exposures enable us to see several direct transitions between different classes of variability. We focus on the connection between the behavior of GRS 1915+105 at X-ray energies and at radio wavelengths. The data are studied in a model independent manner through the source light curves, its hardness ratio, and color color diagrams. During a period of steady "hard" X-ray state (the so-called class χ) we observe a steady radio flux. This is interpreted as the signature of the presence of a compact jet. We then turn to 3 particular observations during which we observe several types of soft X-ray dips and spikes cycles, followed by radio flares. During these observations GRS 1915+105 is in the so-called ν, λ, and β classes of variability. The observation of ejections during class λ are the first ever reported. Our model independent approach of the high energy data allows us to generalize the fact that a (non-major) discrete ejection always occurs, in GRS 1915+105, as a response to an X-ray sequence composed of a spectrally hard X-ray dip (more pronounced at soft X-rays) terminated by an X-ray spike marking the disappearance of the hard X-ray emission above 18 keV. This model independent approach also permits us to identify the trigger of the ejection as this X-ray spike. In addition, a possible correlation between the amplitude of the radio flare and the duration of the X-ray dip is found in our data. In this case the X-ray dips prior to ejections could be seen as the time during which the source accumulates energy and material that is ejected later. The fact that these results do not rely on any spectral modelling enhances their robustness.

Subject headings: accretion, accretion disks — black hole physics — stars: individual (GRS 1915+105) — X-rays: binaries — radio continuum: stars

1. INTRODUCTION

Microquasars are the Galactic scaled-down versions of AGNs (Mirabel & Rodríguez 1998). In both classes of systems, the copious emission of energy is thought to originate from the accretion of matter onto the central black hole (BH), which occurs through an accretion disk. Relativistic ejections are observed in both classes of objects, either through discrete jets, or in a self-absorbed compact jet. Apart from morphological similarities, the difference of the mass of the central object leads to a higher temperature of the inner regions of the accretion disk in the Galactic sources, smaller extent of the jets, and, of high importance, smaller time scales in any of the phenomena associated to either accretion or ejection processes (Mirabel & Rodríguez 1998). As a result, microquasars are excellent laboratories to study the accretion-ejection links on time scales from seconds to days. This is done by coupling the variations seen at X-ray energies (mapping the regions closest to the compact object) to those seen at radio and infrared (IR) wavelengths (representing the emission from the jets). Such a work has been initiated in GRS 1915+105 (Pooley & Fender 1997; Eikenberry et al. 1998; Mirabel et al. 1998; Fender & Pooley 1998), and pursued in a large number of systems since then.

An extensive review on GRS 1915+105 can be found in

[1]Laboratoire AIM, CEA/DSM - CNRS - Université Paris Diderot, DAPNIA/SAp, F-91191 Gif-sur-Yvette, France
[2]Observatory, PO Box 14, FI-00014 University of Helsinki, Finland
[3]School of Physics and Astronomy, University of Southampton, SO17 1BJ, UK
[4]Astrophysics, Cavendish Laboratory, J J Thomson Avenue, Cambridge CB3 0HE, UK
[5]Service d'Astrophysique, (UMR AstroParticules et Cosmologie), CEA Saclay 91191 Gif-sur-Yvette, France
[6]European Southern Observatory, Chile. On leave from CEA-Saclay, France
[7]INAF-Osservatorio Astronomico di Brera, via Bianchi 46, 23807 Merate, Italy
[8]European Space Astronomy Centre (ESAC) Apartado/P.O. Box 78, Villanueva de la Cañada, E-28691 Madrid, Spain
[9]Danish National Space Center, Technical University of Denmark, Juliane Maries Vej 30, 2100 Copenhagen, Denmark
[10]Tuorla Observatory and Department of Physics, University of Turku Väisäläntie 20, FI-21500 Piikkiö, Finland
[11]IASF Milano-INAF, Via Bassini 15, 20133 Milano, Italy
[12]LAOG, Université J. Fourier (UMR5571), Grenoble, France

Fender & Belloni (2004). To summarize, GRS 1915+105 hosts a BH of 14.0±4.4 $M_\odot$ (Harlaftis & Greiner 2004), it is one of the brightest X-ray sources in the sky and a source of superluminal ejections (Mirabel & Rodríguez 1994), with true bulk velocity $\geq$ 0.9c. From these superluminal motions an upper limit on the distance to GRS 1915+105 of 11.2 kpc could be derived (on the assumption of intrinsic symmetry in the bipolar jets Fender et al. (1999)), although a distance as low as 6 kpc (Chapuis & Corbel 2004) cannot be excluded. The source is also known to show a compact jet during its periods of low and steady level of X-ray emission (Dhawan, Mirabel & Rodríguez 2000).

GRS 1915+105 has been extensively observed with the *Rossi X-ray Timing Explorer* (*RXTE*) since 1996. A rich pattern of variability has emerged from these data with time scales from years down to 15 ms (e.g. Morgan, Remillard & Greiner 1997). Belloni et al. (2000), analyzing 163 *RXTE* observations from 1996–97, classified all the observations into 12 separate classes (labeled with greek letters) based on count rates and color characteristics. This scheme has been widely used ever since and is also applied here. The classes could be interpreted as transitions between three basic states (A-B-C): A being equivalent to the Soft State, B to the Soft Intermediate State and C to the Hard Intermediate state in the classification of Homan & Belloni (2005). These spectral changes are, in most of the classes, interpreted as reflecting the rapid disappearance of the inner portions of an accretion disc, followed by a slower refilling of the emptied region (Belloni et al. 1997). Note that other possibilities as the disappearance of the corona (Chaty 1998; Rodriguez et al. 2002b; Vadawale et al. 2003), or dissipation of magnetic energy (e.g. Tagger et al. 2004) have also been invoked in some models.

Multi-wavelength coverages involving radio, IR and X-ray telescopes have shown a clear but complex association between soft X-rays and radio emission, including radio QPOs in the range 20–40 min which were associated with X-ray variations on the same time scale (Pooley & Fender 1997; Eikenberry et al. 1998; Mirabel et al. 1998; Fender & Pooley 1998). These oscillations were ascribed to small ejections of material from the system, and were found to correlate with the disk instability, as observed in the X-ray band. This was the first time that the disk-jet relation could be studied in detail. This kind of cycle could also reflect some magnetic flood scenario in which reconnection events would allow the ejection of blobs of material (Tagger et al. 2004).

While fine X-ray spectral and temporal analysis will be presented in a companion paper (Rodriguez et al. 2007 hereafter paper 2), we analyze here , in a model independent way, the multi-wavelength data from our 2 years monitoring campaign focusing on the observations during which correlated X-ray and radio variabilities are seen. We start with giving the basic properties of our *INTEGRAL* observations, i.e. we describe the campaign and the data reduction processes in section 2. In section 3 and 4 we describe and discuss the four observations from which strong radio/X-ray connections are observed.

2. OBSERVATIONS AND DATA REDUCTION

2.1. *Journal of the observations*

The journal of the *INTEGRAL* observations belonging to our monitoring campaign taken from 2004 October to 2005 December is given in Table 1, while Table 2 reports the details of our simultaneous *RXTE* monitoring. The daily multiwavelength light curves of GRS 1915+105 as seen by *RXTE*/ASM (1.2-12 keV), the Ryle Telescope (RT, 15 GHz) over the period of interest are reported in Fig. 1 (January 1st 2004 is MJD 53 005). The days of our *INTEGRAL* pointings are shown as vertical arrows, the four bigger ones indicate the four observations whose accretion ejection properties are discussed in more detail in this paper.

2.2. *INTEGRAL data reduction*

Our monitoring makes use of the *INTEGRAL* Soft Gamma-Ray Imager (ISGRI, Lebrun et al. (2003)) – the low energy detector of the Imager On-Board *INTEGRAL*(IBIS) – to cover the 18 to $\sim$ 300 keV energy range, and the X-ray monitors JEM-X (Lund et al. 2003) to cover the 3-30 keV energy range. Both instruments see the sky through a coded mask. We reduced the *INTEGRAL* data using the Off Line Scientific Analysis (`OSA`) v. 7.0. Apart from the different version of the softwares, the data from ISGRI and JEM-X were reduced in a way similar to that presented in Rodriguez et al. (2005) for another source present in the totally coded field of view (TCFOV) of ISGRI, IGR J19140+0951. Our first step was to produce ISGRI images in two energy bands, 20–40 and 40–80 keV, in order to detect the active sources of the FOV which have to be taken into account in the (spectral and temporal) extraction processes. All sources with a signal to noise ratio greater than 6 in the 20–40 keV ranges were considered. The list of sources found in each revolution is given in Table 3. Apart from a purely technical process of obtaining the cleanest data for the main target of our analysis (e.g. Goldwurm et al. 2003, for the details of the IBIS data reduction processes), this procedure also allows us to survey the brightest sources of this field and analyze their data (e.g. analysis of Aql X-1 during its faint April 2005 outburst can be found in Rodriguez et al. (2006))

Since GRS 1915+105 is the main target of all our observations, with an hexagonal dithering pattern it is always in the TCFOV of ISGRI, and in the useful part of the FOV of JEM-X. We, therefore, did not include any restriction concerning the off-axis angle in selecting the data. The second step of our analysis was to produce JEM-X and ISGRI light curves with the view to identify the class, and monitor the behavior of the source on short time scales. The JEM-X light curves were extracted with a time resolution of 1s between $\sim$ 3–13 keV, and further rebinned to 20 s. The ISGRI light curves were extracted between 18–50 keV with a time resolution of 20 s. They were further rebinned as they can be quite noisy and hide interesting patterns when plotted on such a short time bin. The rebinning depended on the brightness of the source at energies above 18 keV and was usually in the range 50–200 s. The instrumental and sky background is estimated on the same time bins as the source raw count rate, from non-illuminated pixels. For ISGRI an additional step is to renormalize this background using background maps provided with the calibration tree. For each instrument, the light curves are corrected for background during the ex-

traction process. From these background corrected light curves we produced softness ratios (SR) defined as SR= 3–13 keV/18–50 keV.

2.3. *RXTE data reduction*

The *RXTE* data were reduced with the `LHEASOFT` v. 6.1.2. All data products were extracted from user's good times intervals (GTI). GTIs corresponded to times when the satellite elevation was greater than 10° above the Earth limb, the offset pointing less than 0.02°, and proportional counter unit #2 was active. In order to identify the classes, we extracted 1s resolution light curves in the 2–60 keV range and in the three energy bands defined in Belloni et al. (2000), from the Proportional Counter Array (PCA). These bands are 2–5.7 keV (channels 0-13, PCA epoch 5), 5.7–14.8 keV (channels 14-35), and >14.8 keV (channels 36-255). The colors were defined as HR1=5.7–14.8/2–5.7 keV and HR2=14.8–60/2–5.7 keV. The shift of gain between the different epochs of PCA leads to different absolute values of the count rates, hardness ratios (HR) and position in the color-color (CC) diagrams, but the general shape of a given class is easily comparable to those of epoch 3 (Belloni et al. 2000), and therefore allowed us to easily identify the class of variability in each observation. 16 s resolution light curves were extracted from standard 2 data between 2 and 18 keV. These were directly compared to the 3–13 keV and 18–50 keV light curves extracted from the *INTEGRAL* data. All these light curves were corrected for background, using the latest PCA background models available for bright sources.

2.4. *Ryle Telescope observations*

The observations with the Ryle Telescope followed the scheme described by Pooley & Fender (1997). Observations, of Stokes' I+Q, were interleaved with those of a nearby phase calibrator (B1920+154), and the flux-density scale set by reference to 3C48 and 3C286, and is believed to be consistent with that defined by Baars et al. (1977). The data are sampled every 8 s, and 5-min averages displayed in this paper. Fig. 1 shows the 15 GHz long term light curve of GRS 1915+105.

3. ACCRETION EJECTION LINKS, AND THE PRESENCE OF X-RAY CYCLES

Although the classification of the X-ray classes is purely phenomenological, we think it is rather important since it helps when referring to a given observation. Furthermore the succession of classes, their relation with the radio behavior, and the pattern of state transition through a single class probably hides rich physical phenomena related to the accretion and ejection mechanisms. Hence, we feel it is important to report the identification of all classes and the possible transitions we observed during our campaign. Since it is not the core of our paper, however, this is given in the Appendix. The classes of variability identified during each observation are reported in Table 3. In the following we focus on the accretion ejection links of Obs. 1, 2, 4, and 5 with particular emphasis on the intervals that respectively belong to classes ν, λ, χ, and β during the times we have simultaneous radio and X-ray coverages (see Appendix).

3.1. *Observation 1: class ν*

As can be seen on Fig. 2 on two occasions, at least, a sequence of > 100 s long X-ray dip ended by an X-ray spike (hereafter cycles) were followed by radio flares indicative of ejection of material (e.g. Mirabel et al. 1998). The cycles are all well defined above 18 keV (Fig. 2), with almost identical patterns as in the soft X-rays although the dip and spike have an amplitude less marked. A notable difference with the soft X-ray light curve, however, is the presence of a short dip close to the spike. The shapes of the two radio flares are similar (Fig. 2). To estimate their true amplitude above a noise level, we estimated the variance of the radio light curve when in the non-flare intervals. The typical RMS was 3.0 mJy. The flares reached maxima (calculated from the light curve with a temporal resolution of 5 min) of 62 ± 3 mJy and 60 ± 3 mJy on MJDs 53296.76 and 53296.83 respectively. Radio flares have been seen to occur as a response to each sequences of X-ray dips-spikes in this particular class (Klein-Wolt et al. 2002).

3.2. *Observation 2: class λ*

As can be seen on Fig. 3, and Fig. 4, on one occasion, an X-ray cycle was followed by a radio flare indicative of an ejection event (e.g. Mirabel et al. 1998). The shape of the flare is rather symmetric. To estimate the statistical significance of the flare, we calculated the variance of the first part of the radio light curve. From this we can calculate a typical RMS of 2.3 mJy. The flare thus had an amplitude of 40 ± 2.3 mJy (in the 5min bins light curve Fig. 4). This observation of a radio flare during a class λ is the first ever reported. As for the other classes with cycles, e.g. class ν, the dips of class λ are known to be spectrally hard (Belloni et al. 2000). This is obvious in the SR of Fig. 4. The dip, here mainly visible at soft X-rays, ended with a soft X-ray spike, corresponding to a sudden decrease of the > 18 keV emission (Fig. 4).

Interestingly, two small radio flares seem to have occured prior to the main one around MJDs 53324.68 and 53324.75 (Fig. 4). They had respective amplitudes of 15.1 and 11.3 mJy. The flares were then significant at respectively 6.5 and 4.9 σ. Deep inspection of the X-ray light curve shows that they followed short X-ray dips that occured around MJD 53324.66 and MJD 53324.72 (Fig. 4). Unfortunately, during the first X-ray dip, for which the decrease of the 3–13 keV count rate is clearly visible (Fig. 4), *INTEGRAL* did a slew between two subsequent pointings that prevented a full coverage of this interval. We can just set a lower limit on the duration of the dip of 100s. In the second case, the delay between the return to a high degree of variability at X-ray energies and the peak of the radio flare was 0.15 hours. Although the cycle was shorter than during the long one preceding the 40 mJy flare, a similar sequence of event can be seen here. The dip is really apparent below 13 keV and is spectrally hard as illustrated by the SR on Fig. 4. The cycle ended with a return to a high level at soft X-rays associated with a slight decrease of the hard X-ray emission. As in the previous cases the cessation of the dip manifested by a peak (although of much smaller amplitude than in the main cycle) in the SR Fig. 4.

3.3. *Observation 4: class χ*

Contrary to the previous classes, GRS 1915+105 showed a relatively steady emission at all wavelengths, although some variations, in particular near the end of the observation are visible (Fig. 5). In the radio domain the source had a mean flux of 44.9 mJy with a typical RMS of 3.0 mJy (calculated from the radio light curve with a binning of 5 min) from MJD 53473.10 to MJD 54473.24. It then slowly increased during $\sim$ 4800 s to reach a mean flux of 70.4 mJy, with a RMS of 4.4 mJy from MJD 53473.30 to 53473.42. The mean 3–13 keV JEM-X was 115.7±6.8 cts/s from MJD 53473.10 to 54473.24 and 107.3±6.5 cts/s later (MJD 53473.30–53473.42). The mean 18–50 keV ISGRI count rates was 55.3±2.8 cts/s from MJD 53473.10 to 54473.24 and 58.4±2.7 cts/s after (MJD 53473.30–53473.42).

Near the end of the observation (MJD 53474.4), the radio flux was still around the same value as before the radio coverage was stopped (Fig. 5). It decreased for a short time to $\sim$ 59 mJy and increased to $\sim$ 110 mJy after MJD 53472.2. Note that an inspection of the radio light curve the following days, showed that the radio flux was at approximately the same level (120-130 mJy) on MJD 53477, and had decreased to $\sim$ 60 mJy on MJD 53478. This may suggest that the radio emitter, the jet, has persisted over a long period, although it showed slight variations in its strength.

3.4. *Observation 5: class μ and β*

During this observation, again on two occasions, the X-ray dips were followed by radio flares with symmetric shapes (Fig. 6). The radio flares reached their maxima on MJDs 53504.248 and 53504.298 respectively, with absolute peak fluxes of 58.5 and 68.3 mJy (when using 5 min bins to estimate them). Unlike the two other classes, they, however, sat on top of a non-zero radio flux. The mean radio flux prior to the two flares was 35.2 mJy with an RMS of 3.4 mJy. The net amplitude of the flares above the continuum emission was therefore 23.3 ± 3.4 mJy and 33.1 ± 3.4 mJy, for the first and second flares respectively. The time delays between the X-ray spikes half way through the dips (the triggers of the ejections, Mirabel et al. (1998); Chaty (1998)), and the radio maxima were $\sim$ 0.31 hour and $\sim$ 0.34 hour respectively. The presence of a relatively high radio flux prior to the ejections, when GRS 1915+105 was showing a high level of very variable X-ray emission (Fig. 6), is quite interesting. This kind of steady radio flux is usually indicative of the presence of a compact jet. The latter is, however, usually seen when the source shows a steady X-ray flux dominated by hard X-ray emission, its spectrum being, then, indicative of a hard-intermediate state (state C of Belloni et al. (2000)), similar to the one seen during Obs. 4. Klein-Wolt et al. (2002) also report the presence of radio emission during class μ observation with no oscillations of the radio flux. This could indicate that the cycles in class μ are too fast to be detected at radio wavelength. We should also note that the radio non-zero continuum seems to be the tail or exponential decay of a major flare that occured some days before the observation as can be seen in Fig. 1. As in classes ν and λ, the cycles are also well defined above 18 keV. In particular, a dip can clearly be seen at hard X-ray energies during each cycle.

4. DISCUSSION

We have presented the results of 2 years of simultaneous monitoring campaigns on the Galactic microquasar GRS 1915+105 made with several instruments. This has allowed us to follow the behavior of the source from radio wavelengths to hard X-ray energies. The *INTEGRAL* observatory, thanks to its large field of view, has allowed us to quickly monitor the behavior of sources that are in the vicinity of GRS 1915+105.

In the case of GRS 1915+105, we first classified the X-ray classes of variability of the source (Appendix), and saw that GRS 1915+105 could undergo transitions through many classes of variability on short time scales (few hundreds seconds, Appendix). We report here the following specific and direct transitions: $\nu \leftrightarrow \rho$ (Obs. 1), $\mu \leftrightarrow \lambda$ and $\mu \rightarrow \delta$ (Obs. 2), $\mu \rightarrow \beta$ (Obs. 5), $\phi \rightarrow \theta \rightarrow \delta$ (Obs. 7), $\chi \leftrightarrow \theta$ (Obs. 8 & 9, Ueda et al. 2006), possibly $\delta(?) \rightarrow \mu \rightarrow \beta$ (Obs. 10), and $\delta \rightarrow \mu \rightarrow \beta$ (Obs. 11). We then focused more particularly on 3 observations showing the occurrences of X-ray cycles followed by radio flares. In a fourth observation the source was in its steady "hard" state accompanied by the presence of a persistent radio emission.

4.1. *Steady radio and X-ray emission*

During Obs. 4, the persistent radio emission can be safely attributed to a steady compact jet, although the lack of simultaneous coverage at other radio wavelengths prevents us to precisely estimate the radio spectral index. GRS 1915+105 is in a class χ also known as being its "hard" state (in fact it rather corresponds to a hard-intermediate state in the recent classification of Homan & Belloni (2005)), a state during which strong radio emission associated to a compact jet has been seen in the past (e.g. Fuchs et al. 2003). During this particular observation, the radio flux increased by a factor of 1.57 in a rather short time (less than an hour), while the 3–13 keV and the 18–50 keV count rates remained constant at the 1-σ level. The fact that the X-ray count rates do not follow the evolution of the radio flux may indicate that the jet has no influence on the X-ray emission at all. However, GRS 1915+105 is a source known to follow the radio to X-ray correlation seen in many microquasars (Corbel et al. 2003; Gallo 2006), which has been widely interpreted as evidence for an influence of the jet at X-ray energies. A way to reconcile our observation to the latter interpretation is to suppose that the X-ray count rates come from "competing" media emitting in the same energy ranges, e.g. a disk, and/or a standard corona and/or the jet. A model-dependent analysis is, however, beyond the scope of this paper.

4.2. *On the generalization of the radio to X-ray connection*

Focusing on the observations showing X-ray cycles, the observations of links between the X-ray cycles in class ν and β confirm previous findings that such events seem to be generic in those classes (Pooley & Fender 1997; Mirabel et al. 1998; Klein-Wolt et al. 2002). The observation of radio ejection in the λ class of variability is, however, the

first ever reported. This may suggest a generalization of the fact that small amplitude ejections in GRS 1915+105 always occur as a response to X-ray cycles providing the X-ray hard dip is long enough (Klein-Wolt et al. 2002). The observation by Feroci et al. (1999) of an X-ray dip not followed by a radio flare during a *BeppoSax* observation may be in contradiction with this generalization.

In fact, although some obvious morphological differences exist between the different classes, in term of SR and colors they all undergo similar evolutions (Belloni et al. 2000, and Fig.7). The cycles always begin with a transition to a low flux below 13 keV, the X-ray dip (interval I in Fig.7), associated to a relatively bright flux above 18 keV. The 3–13 keV/18–50 keV SR has then a value of about 1. This indicates the dip is spectrally hard. A short spike (interval II) occurs in the 3–13 keV range (it is very short in class λ). This spike seems to be the onset of a sudden and fast change, as the rising part is still hard (SR$\sim$ 1), although it smoothly evolves. After the spike, however, a fast and important decrease of the hard X-ray emission (interval III) during which the SR increases greatly, indicates a much softer state is reached. In class ν, for example, the 18–50 keV count rate decreases by a factor $\sim$3. The evolution of the soft X-ray emission is less dramatic, although it decreases as well from interval II to III in all classes, its evolution seems to be the continuation of the slow increase seen in each case at the end of interval I (Fig. 7). Mirabel et al. (1998); Chaty (1998) identified the spike (II) in class β as the trigger to the ejection later seen in radio. In all three cases the delay between Int. II seen at X-ray energies and the peak of the radio flare is very similar. In class ν it is respectively ~ 0.31 hour and ~ 0.29 for the first and second flares respectively. In class λ, it is ~ 0.31 hour, while in class β it is respectively $\sim$ 0.31 hour and $\sim$ 0.34 hour for the first and second flare. This similarity may suggest that the same physical mechanism in the three classes give rise to the same phenomenon. Hence if the spike (Int. II) in class β is indeed the trigger of the ejection, it has the same role in classes ν and λ. This model independent approach may suggest that the ejected material is the material responsible for the hard X-ray emission prior to the ejection occuring at Int. II. A similar interpretation was given by Chaty (1998) and Rodriguez et al. (2002b) in the case of class β and α observations.

The lack of ejection after the X-ray dip reported by Feroci et al. (1999) can then easily be understood. In their case the dip in question is not followed by a spike, while an ejection they observe follows an X-ray spike, possibly following an X-ray dip (but missed due to occultation of GRS 1915+105 by the Earth). Interestingly, the approximate delay between the X-ray spike and the maximum of the radio flare in this observation (taken in 1996, Feroci et al. (1999)) is ~ 0.28 hour, hence very similar to what we obtain in all our cases. In addition, the X-ray dip discussed in Feroci et al. (1999) seems much softer than the remaining intervals of their observation (see Table 1 of Feroci et al. 1999), as its photon index is the softest of the sequence. Putting everything together, it seems, then, that we can generalize the following: plasmoid ejections *always* occur as response to an X-ray sequence composed of *a longer than 100s spectrally hard X-ray dip terminated by a short X-ray spike*, the latter being the trigger of the ejection. This possible generalization is even re-inforced by the observation of smaller amplitude ejections following short cycles during class λ. Although the shorter duration of the events prevented us to obtain the same details as in the main cycles, it is obvious from Fig. 4 that GRS 1915+105 undergoes similar evolution during one of the shorter dips. In particular, the dip is spectrally hard (SR$\sim$ 1), while it ends with a small 3–13 keV spike, also visible in the SR which increases to about 9, and therefore marks a transition to a much softer state.

4.3. *A link between the radio amplitude and the duration of the X-ray dip?*

Looking at class λ in more detail, we detected the presence of two small radio flares each apparently following an X-ray dip of short duration. In order to study a possible dependence of the amplitude of the radio flare on the duration of the X-ray dip, we estimated the duration of the X-ray dips in each class. Since the dips have different shape, and the transition into the dip is quite smooth, the true starting time of the dip is quite difficult to estimate. To do so, we take as the starting point of the dip the mean time between the highest point immediately preceding the transition to the dip and the time at which the bottom of the dip is truly reached. The error is here the time difference between the highest point immediately preceding the transition to the dip and the bottom of the dip. The end time is taken as the "foot" of the X-ray spike which renders its identification easier, given that the transition into the spike is quite sudden and rapid in all cases. The results are plotted in Figure 8. A positive correlation between the two quantities is quite obvious. The linear Spearman correlation coefficient is 0.93. The best linear fit leads to $F_{15\ \mathrm{GHz}}(\mathrm{mJy}) = 0.025 \times t(\mathrm{s}) + 17.2$. Note, however, that a pure linear dependence of the radio amplitude vs. the duration of the X-ray dip remains unlikely as Klein-Wolt et al. (2002) remarked that for an ejection to take place a dip of minimum duration ~ 100 s is necessary.

In order to populate the region around 1000 s, we searched the literature for simultaneous radio (15 GHz) and X-ray data showing the occurrences of cycles, and ejections. Some clear examples are given in Pooley & Fender (1997) and Klein-Wolt et al. (2002), for a total of 8 cycles occuring around MJDs 50381.6, 50698.8, and 51342.1. However, in 4 cycles (on MJDs 50698.76 50698.78, 51342.06 51342.12) the radio flares sat on top of non-zero (30 to 60 mJy) radio continuum which renders the estimate of the radio amplitude very uncertain. Note that the binning of 32 s presented in Klein-Wolt et al. (2002) is also another source of uncertainty. These four cycles are not included here. The radio flares around MJD 50381.6 (Pooley & Fender 1997) also sat on a non zero continuum, but the latter is quite weak ($\sim$ 10 mJy), and therefore the amplitude of the radio flare can be estimated more accurately. Finally the last radio flare, occurs on MJD 50698.83 just after a period of $\sim$0 mJy level. These four additional cycles are added in Fig. 8, and represented as triangles. With these new points, the general tendency remains the same. The linear Spearman correlation coefficient is 0.90, and the best linear fit leads

to $F_{15\ \mathrm{GHz}}(\mathrm{mJy}) = 0.022 \times t(\mathrm{s}) + 20.7$.

We also searched for other possible correlations between some properties of the cycles, and the amplitude of the radio flares, as, e.g., the amplitude of the spike (with respect to the bottom of the preceding dip), the amplitude of the variations of the SR after the spike, or the time delay between the X-ray spike and the peak of the radio flare. We do not find any obvious correlations between any of these quantities. The maximum variation for the SR is seen during the main λ cycle, while it corresponds to a rather low amplitude ejection. No correlation is either found between the amplitude of the spike and the amplitude of the radio flare. The maximum amplitude of the spike occurs during the main cycle of class λ observation, for a relatively low amplitude radio flare. The spike with the minimum amplitude occurs during class β observation for a radio flare of similar amplitude to that of class λ.

The correlation of the radio amplitude with the duration of the X-ray dip brings interesting possibilities regarding the accretion-ejection links. This may indicate, for example, that during the X-ray dip energy and matter, later used to power the ejection, are accumulated. The longer the X-ray dip, the more energy and/or matter are accumulated, and then the higher is the radio amplitude. This is compatible with the fact that the ejected material is the matter responsible for the hard X-ray emission suggested by the sudden decrease of the 18–50 keV emission at the spike. In that case, a longer duration of the dip would indicate that more matter, later ejected, is accumulated during the dip.

Another possible explanation (not exclusive with the previous one) relies on the so-called 'Magnetic Floods' scenario/model (Tagger et al. 2004). This model was recently proposed to account for the observed accretion-ejection and quasi-periodic variability properties, during the cycles observed in a class-β observation. In this scenario, during the X-ray dip an 'Accretion-Ejection Instability' (AEI, Tagger & Pellat (1999)) develops (and replaces the Magneto-Rotational Instability (MRI) thought to occur during the preceding luminous soft X-ray state), because poloidal magnetic field advected with the matter has accumulated in the inner region of the disk. If the magnetic configuration is favorable, a sudden reconnection event (producing the spike) can occur between magnetic fields of opposite polarities in the disk and in the magnetospheric structure of the black hole. This would then lead to the dissipation of the accumulated field in the inner regions, leading to the ejection (of the corona), and return to the MRI (Tagger et al. 2004). This scenario had some success in explaining all observational signatures (including QPOs) seen during the particular class β these authors dealt with. This interpretation is also compatible with the observed behavior we present here, and, in particular, the possible correlation between the amplitude of the radio flare and the duration of the dip (Fig. 8). In that case, the longer the dip, the more magnetic flux can be accumulated in the inner region, and again the higher is the available energetic reservoir used in energizing the ejection. This interpretation is however only tentative, and should not hide the fact that other models may explain these observations. However, the generalization of the X-ray cycles to radio ejections and the relation between the duration of the dip and the amplitude of the ejection bring strong constraints on any attempt to model the accretion-ejection behavior in GRS 1915+105 and other microquasars. Note that the possible correlation we found here clearly needs to be confirmed through systematic inspection of simultaneous radio and X-ray data, but also adding different frequencies (e.g. IR data).

J.R. would like to thank S. Chaty for useful discussions, C.A. Oxborrow for invaluable help with the ISGRI and JEM-X data reduction and calibration, and A. Gros, A. Sauvageon and N. Produit on specific aspect of the *INTEGRAL* software. J.R. also acknowledges E. Kuulkers, and more generally the *INTEGRAL* and *RXTE* planners for their great help in scheduling the observations. D.C.H. gratefully acknowledges a Fellowship from the Finnish Academy. AP acknowledges the Italian Space Agency financial and programmatic support via contract ASI/INAF I/023/05/0. The authors thanks the referee for his carefull reading and valuable report which helped to greatly improve the quality of this paper.
Based on observations with *INTEGRAL*, an ESA mission with instruments and science data centre funded by ESA member states (especially the PI countries: Denmark, France, Germany, Italy, Switzerland, Spain), Czech Republic and Poland, and with the participation of Russia and the USA. This research has made use of data obtained through the High Energy Astrophysics Science Archive Center Online Service, provided by the NASA/ Goddard Space Flight Center.

REFERENCES

Baars, J.W.M., Genzel, R., Pauliny-Toth, I.I.K., Witzel, A. 1977, A&A 61, 99
Belloni, T., Mendez, M., King, A. R., et al. 1997, ApJ, 488, 109
Belloni, T., Klein-Wolt, M., Mendez, et al. 2000, A&A, 355, 271
Chapuis, C. & Corbel, S. 2004, A&A, 414, 659
Chaty, S. 1998, Thèse de Doctorat, Université Paris 7
Corbel, S., Nowak, M. A., Fender, R. P., Tzioumis, A. K., Markoff, S. 2003, A&A, 400, 1007
Dhawan, V., Mirabel, I.F. & Rodríguez, L.F., 2000, ApJ, 543, 373
Eikenberry, S.S., Matthews, K., Morgan, E.H., Remillard, R.A., Nelson, R.W. 1998, ApJ, 494, L61
Fender, R. & Pooley, G. 1998, MNRAS, 300, 573
Fender, R.P. et al. 1999, MNRAS, 304, 865.
Fender, R.P. & Belloni, T. 2004, ARA&A, 42, 317
Feroci, M., Matt, G., Pooley, G., et al. 1999, A&A, 351, 985
Fuchs, Y., Rodriguez, J., Mirabel, F., et al. 2003, A&A, 409, L35.
Fritz, S., Kreykenbohm, I., Wilms, J., et al. 2006, A&A, 458, 893.
Gallo, E. 2006, in "Proceedings of the VI Microquasar Workshop: Microquasars and Beyond", PoS(MQW6)009
Goldwurm, A., David, P., Foschini, L., et al. 2003, A&A, 411, L223
Harlaftis, E.T & Greiner, J., 2004, A&A, 414, 13.
Homan, J. & Belloni, T. 2005, Ap&SS, 300, 107
Klein-Wolt, M., Fender, R. P.; Pooley, G. G., et al. 2002, MNRAS, 331, 745
van der Laan, H. 1966, Nature, 211, 1131
Lebrun, F., Leray, J.-P., Lavocat, P., et al. 2003, A&A, 411, L141
Lund, N., Budtz-Jørgensen, C., Westergaard, N.J., et al. 2003, A&A, 411, L231
Mirabel, I.F. & Rodríguez, L.F. 1994, Nature, 371, 46
Mirabel, I.F. & Rodríguez, L.F. 1998, Nature, 392, 673
Mirabel, I.F., Dhawan, V., Chaty, S., et al. 1998, A&A, 330, L9
Morgan, E.H., Remillard, R.A & Greiner, J. 1997, ApJ, 482, 993
Pooley, G.G, & Fender, R.P. 1997, MNRAS, 292, 925

Rodriguez, J.,Varnière, P., Tagger, M., Durouchoux, P., 2002a, A&A, 387, 487
Rodriguez, J., Durouchoux, P., Tagger, M., et al., 2002b, A&A, 386, 271..
Rodriguez, J., Cabanac, C., Hannikainen, D.C., et al. 2005, A&A, 432, 235
Rodriguez, J. & Shaw, S.E. 2005, ATel 660
Rodriguez, J., Shaw, S.E. & Corbel, S. 2006, A&A, 451, 1045
Rodriguez, J., et al. 2007, submitted to ApJ, **paper 2**
Shimura, T., & Takahara, F. 1995, 445, 780
Tagger, M., Pellat, R. 1999, A&A, 349, 1003
Tagger, M., Varnière, P., Rodriguez, J. & Pellat, R. 2004, ApJ, 607, p. 410
Ueda, Y., Ishioka, Sekiguchi,K., Ribo, M., Rodriguez, J., et al. 2006, in "Proceedings of the VI Microquasar Workshop: Microquasars and Beyond", PoS(MQW6)023
Vadawale, S.V., Rao, A.R., Naik, S., et al. 2003, ApJ, 597, 1023

APPENDIX

IDENTIFICATION OF THE X-RAY CLASSES

In all cases the identification of states is based on the simultaneous inspection of the JEM-X light curves for the general shape, and PCA (when available) for confirmation through inspection of the CC diagrams. The different responses of JEM-X and PCA prevent direct comparison of the CCs produced with the 2 instruments, as they lead to completely different patterns. In some cases, especially when no simultaneous coverage by *RXTE* is available we identify the class as the most likely based on the resemblance with the patterns identified by Belloni et al. (2000). The multiwavelength light curves and CC diagrams are reported in Fig. 2 to 6 for the four observations discussed in details in the paper and 10 to 14 for the others. As can be seen, while *RXTE* gives an easy access to high time resolution light curves and CC diagrams, *INTEGRAL* allows us to have a continuous coverage of the source and thus study the evolution of classes while witnessing transition between some of them.

Obs. 1 (Fig. 2) shows alternating X-ray dips and spikes (cycles), followed by intervals of high level of X-ray flux at all energies, and variability of different duration. Deep inspection of these behaviors shows that the source was in an alternation of class ν and class ρ-heartbeat, as illustrated in Fig. 2. As mentioned by Belloni et al. (2000), each ν-type cycle is separated by the preceding one by an interval of ρ type behavior. This is illustrated by the fact that the CC diagram (Fig. 2) of the class ν shows the same pattern as the one from class ρ with an extension towards higher values of HR2, corresponding to the dips. The radio light curve shows that at least after two sequences of X-ray dip/spike (hereafter cycles) radio flares occured. In the past, similar radio flares have been seen to occur after each cycle (e.g. Klein-Wolt et al. 2002). This observation is one of the four whose deep analysed is presented in the core of this paper.

Obs. 2 (Fig. 3) shows a high level of very variable X-ray emission. On some occasions, one can see short dips in the soft X-ray light curves each followed by a spike. A very variable behavior is also seen at hard X-ray energies, with occurrences of short dip clearly visible in the 18–50 keV light curve (Fig. 3). Looking more carefully at the source light curves, one can see that GRS 1915+105 seems to transit between different classes as illustrated by the *RXTE* intervals (Fig. 3). Inspection of the CC diagrams shows that it started in class μ, transited to a class λ, transited back to μ, and evolved to a class γ. The presence of short $\sim$ 100s long X-ray dips visible in the *INTEGRAL*/JEM-X light curves indicate the source transits continuously from μ to λ. Deep analysis of this observation is presented in the core of this paper.

In Obs. 3 (Fig. 9) GRS 1915+105 was in a low luminosity steady state. The 3-13 keV JEM-X count rate was around 110 cts/s, while the 18–50 keV count rate was around 80 cts/s, with a slight decrease to about 70 cts/s near the end of the observation. The 2–18 keV PCA count rate was around 1800 cts/s. All light curves show a high degree of rapid variability. Both the light curve and the CC diagrams indicate the source was in class χ. No RT were performed during this interval. The values of HR1 and HR2 are indicative of a very hard class χ (Fig. 9). In particular, the source is much harder here than during Obs. 4, although both observations belong to the same class.

Obs. 4 (Fig. 5) is very similar to Obs. 3 although GRS 1915+105 was slightly fainter at hard X-ray energies and showed lower values of the HRs. Near MJD 53474.1 the source fluxes increased suddenly. This indicates it underwent a transition to a brighter class, confirmed by the variations of the ASM light curve (Fig. 1). Simultaneous coverage at radio wavelengths shows a rather steady flux at around 50 mJy, although some variations are visible. In particular the radio flux increased up to 100 mJy near the end of the observation (Fig. 5). The global X-ray behavior indicates that GRS 1915+105 was in a radio loud class χ. This observation is one of the four that is deeply analysed in this paper.

Obs. 5 (Fig. 6) shows that GRS 1915+105 was in classes of high X-ray flux with a high degree of variability. It is interesting to note, that the overall 18–50 keV variability increased along the observation. Although the mean 18–50 keV flux remained quite bright around 40–50 cts/s, significant dips and spikes can be seen, some in simultaneity with those seen at soft X-rays. It is clear from Fig. 6 that it transited at least between two such classes. Inspection of the CC diagrams shows that it started in a class μ and finished in class β. Our radio observation shows a roughly constant flux of $\sim$ 40 mJy up to MJD 53504.35 where two radio flares occured after occurrences of dip-spike cycles in the X-ray domain. This observation is one of the four that is deeply analysed in this paper.

Obs. 6 was of poor quality due to the effects of high solar activity and was therefore not considered in this analysis.

Obs. 7 (Fig. 10) shows a clear transition from a class with a very low level of X-ray emission, to a class of high flux, with high variability with similar evolving patterns at both soft and hard X-rays. The change from the first class to the last seems to occur through a third one, as illustrated by the differences in the JEM-X and ISGRI light curves, but the lack of *RXTE* data during this interval prevents us to obtain any clear identification. A zoom on the intermediate part (Fig. 11) shows occurences of 3–13 keV "M-shape" patterns typical of class θ. In the mean time, the 18–50 keV light curve shows similar variability (the "M" can be seen in coincidence with those occurring at soft X-rays) and a high variability. The SR indicates the source was hard during the dips of the "M", which is in agreement with the known behavior of class θ(Belloni et al. 2000). This class shows a behavior very similar to other classes with cycles, i.e. spectrally hard dips ended by a soft X-ray spike marking the disappearance of the hard X-ray emission (and transition to a soft state as illustrated by the variations of the SR visible in Fig. 11). The level of radio emission was quite low, with some variability, which is also in agreement with GRS 1915+105 being in class θ (Klein-Wolt et al. 2002). This may further corroborates the generalization of the X-ray to radio connection presented in this paper, although the resolution at radio wavelength do not allow us to identify any radio flares. The analysis of the *RXTE* data of the begining and end of the *INTEGRAL* observations (Fig. 10) indicates that GRS 1915+105 started in class ϕ and ended in class δ.

Obs. 8 & 9 (Fig. 12) were part of a large multi-wavelength campaign involving at high energy the *Suzaku* satellite. The *INTEGRAL* light curves are first very similar to the light curves of Obs. 4, which was indeed a class χ. The higher level of soft X-ray emission, and slightly lower level of hard X-ray emission tend to indicate a rather soft class χ. In the second part, a flare occured at the beginning of the observing interval at both soft and hard X-rays. GRS 1915+105 then returned to a rather steady emission, before transiting to a class that showed similar patterns at soft and hard X-rays. The lack of simultaneous *RXTE* coverage prevents to securely identify the class of varibility. A zoom on the JEM-X light curve (Fig. 12) does not show any easily identifiable pattern. Furthermore, the 3–13 keV/18–50 keV SR has a value quite similar to that of Obs. 8 (Fig. 12) and even to Obs. 4 (not shown). Therefore, it seems the source was still in a class χ. Ueda et al. (2006) presented preliminar results of the whole campaign, and they, in particular, showed that GRS 1915+105 started in a class χ showing the presence of a 6 Hz QPO, and transited in a class θ. The class θ, however, occured between both *INTEGRAL* intervals. The mean level of radio emission was 31 mJy until MJD 53660.7 then increased to about 39 mJY during the first radio interval (Fig. 12). The mean level of radio emission during the second interval was about 40 mJy. The shape of the radio lightcurve may suggest that ejection had taken place between the two observing intervals. A simultaneous VLA light curve (Ueda et al. 2006) is also compatible with this interpretation. Ueda et al. (2006) suggested that ejection of material was triggered at the transition from spectral state-C to spectral state-A (hard intermediate to soft state), similar to our interpretation.

Obs. 10 (Fig. 13), shows a complex behavior made of several possible transitions. The radio light curve (Fig. 13) also indicates 2 different behaviors. In the first part (MJD 53676.56 to 53676.99), the mean 15 GHz flux was $\sim$ 40.4 mJy with an RMS of 10.4 mJy . In the second part (MJD 53676.77 to 53676.841), the mean flux was 36.5 mJy, and the variability of the radio emission had increased significantly with an RMS of 19.6 mJy. This increase seems to be correlated to the X-ray behavior. Around MJD 51678.9 a dip at soft X-ray energies associated to a 18–50 keV strong flare occured. The identification of the classes is only based on the shape of the light curves and 3–13 keV/18–50 keV SR, since no *RXTE* data are available. We can distinguish 3 main periods in the light curves. Until MJD 53676.6, the source flux gradually increased and so did the variability. The shape of the JEM-X light curve (Fig. 13, right panel) and the level of radio emission seem to indicate a class χ observation. The low level of hard X-ray emission and the SR, however, do not favor this identification. Fig. 13 (right) shows that GRS 1915+105 was transiting between state with SR$\sim$ 4 and SR$\sim$ 14–15. This behavior is not what is observed in the other class χ observations. This would rather indicate a class with transitions between spectral state-A and state-B of Belloni et al. (2000), possibly class δ, although it was then fainter than the other class δ observations (e.g. Obs. 5) at both soft and hard X-rays. Note that the possible level of radio emission was not what is usually observed in this class Klein-Wolt et al. (2002) which weakens the identification. After MJD 53676.6, the shape resembles that of a class μ (Fig. 13, right panel), before undergoing a dip-spike sequence indicative of a class β. The identification of class μ is compatible with the level of radio emission (Klein-Wolt et al. 2002). It has to be noted that after the occurrence of this cycle, the level of X-ray emission was higher, and more variable than before.Although there were no more occurrences of cycles towards the end of the observation, the X-ray behavior was similar to what is observed during class β between the occurrences of cycles (Belloni et al. 2000) with a high degree of variability.

Obs. 11 (Fig. 14) also shows several transitions. We do not have any radio coverage during this observation. Although our *RXTE* observations arrive late in the *INTEGRAL* coverage (Fig. 14), it seems that during the first part of the observation (up to about MJD 53695), GRS 1915+105 was in the same type of variability. Zooms on the JEM-X and ISGRI light curves during this first part (not shown) indeed indicate similar morphologies. Inspection of the CC diagram of the first sample of the *RXTE* light curve shows the source was in a class δ (Fig. 14, right panel). The following samples show that GRS 1915+105 had changed classe. This is especially indicated by the track in the CC diagram that shows an incursion in the low HR1 region, with an HR2 as high as 0.05. This pattern and the shape of the light curve is what is observed during class μ. However typical class μ, as the one observed during Obs. 3, show a longer extension towards higher value of HR1 (Fig. 3 right panel). This may simply indicate that while in the first hundred seconds of the interval the variations were still similar to δ, GRS 1915+105 evolved towards β in the end, and hence the CC diagram is a mixture

of both, or simply that due to the short length of the interval ($\sim$2500 s) the high values of HR2 are less observed than in typical (>3000s long) intervals. After that, around MJD 53695.1, another transition occured.GRS 1915+105 shows light curves with a high level of X-ray emission and a high degree of variability. The behavior was the same at soft and hard X-rays with occurrences of long dips in both light curves. This is reminiscent of what we saw during Obs. 5 (Fig. 6), with the occurrence of β-like cycles after some times (Fig. 14, right panel).

Table 1

Journal of all the *INTEGRAL* observations of our campaign. The simultaneous RT observations are also indicated.

Obs. #	Revolution #	ObsId	MJD		RT Radio observations	
			Start	Stop	Start	Stop
1	246	02200280001	53296.3730	53297.5848	53296.710	53296.879
2	255	02200280002	53324.2773	53325.5107	53324.519	53324.803
3	295	02200280003	53442.9542	53444.1497	No coverage	
4	305	02200280004	53472.8673	53474.1419	53473.098	53473.417
...	...	...	...	...	53474.085	53474.141
5	315	02200280005	53503.6328	53504.8691	53503.972	53504.353
6	356	03200200001	53626.3852	53627.5983	53626.853	53626.996
7	361	03200200002	53640.3856	53641.5803	53640.870	53640.946
8	367	03200200003	53659.9563	53660.3679	No coverage	
9	368	03200200004	53661.3222	53662.1313	53661.666	53661.879
10	373	03200200005	53676.2472	53677.4881	53676.562	53676.840
11	379	03200200006	53694.2739	53695.4691	No coverage	

Table 2

Journal of the *RXTE* observations of our campaign.

Obs. # (*INTEGRAL* equivalent)	ObsId	MJD start (MJD)	Date (yyyy-mm-dd)
1	90105-03-02-00	53296.387	2004-10-18
1	90105-03-02-01	53296.593	2004-10-18
1	90105-03-02-02	53296.661	2004-10-18
1	90105-03-02-03	53296.728	2004-10-18
1	90105-03-02-04	53296.794	2004-10-18
1	90105-03-01-000	53297.039	2004-10-19
1	90105-03-01-00	53297.370	2004-10-19
1	90105-03-03-00	53297.440	2004-10-19
1	90105-03-03-01	53297.508	2004-10-19
1	90105-03-03-02	53297.576	2004-10-19
2	90105-05-01-00	53324.261	2004-11-15
2	90105-05-02-00	53324.524	2004-11-15
2	90105-06-01-00	53325.180	2004-11-16
2	90105-06-02-00	53325.442	2004-11-16
3	90105-05-03-00	53442.968	2005-03-13
3	90105-05-03-01	53443.037	2005-03-14
3	90105-05-03-02	53443.105	2005-03-14
3	90105-05-03-03	53443.242	2005-03-14
3	90105-05-03-04	53444.019	2005-03-15
3	90105-05-03-05	53444.089	2005-03-15
4	90105-07-01-00	53472.921	2005-04-12
4	90105-07-02-00	53473.054	2005-04-13
4	90105-07-03-00	53473.972	2005-04-13
5	90105-08-01-00	53503.669	2005-05-13
5	90105-08-02-00	53503.870	2005-05-13
5	90105-08-03-00	53504.719	2005-05-14
7	90105-04-01-00	53640.390	2005-09-27
7	90105-04-02-00	53641.111	2005-09-28
7	90105-04-03-00	53641.439	2005-09-28
7	90105-04-03-01	53641.516	2005-09-28
11	90105-06-03-01	53694.908	2005-11-20
11	90105-06-03-00	53695.039	2005-11-21
11	90105-06-03-02	53695.308	2005-11-21

Table 3

"Quick-look" results of our campaign: list of sources detected by ISGRI (with a signal to noise ratio greater than 6) and classes of variability of GRS 1915+105 in each observation.

Obs. #	Rev. #	Source	Flux (cts/s) 20-40 keV	Flux (cts/s) 40-80 keV	20-40 keV significance (σ)	classes
1	246	GRS 1915+105	37.5	11.0	669	ν,ρ
...	...	H 1907+097[a]	2.7		49	
...	...	4U 1909+07	1.2	0.34	20	
...	...	Ser X-1	1.4		13	
...	...	XTE J1855−026	1.3		6.4	
...	...	SS 433	0.4		6.1	
2	255	GRS 1915+105	19.5	5.4	355	μ, λ, δ
...	...	H 1907+097[a]	1.8		30	
...	...	IGR J19140+0951	1.7	0.64	29	
...	...	4U 1909+07	1.4	0.4	24	
...	...	XTE J1855−026	2.5		13	
...	...	Ser X-1	1.2		11	
...	...	IGR J18483−0311	2.5		9	
3	295	GRS 1915+105	37	7.7	646	χ
...	...	4U 1909+07	1.6		26	
...	...	H 1907+097[a]	1.4	0.43	24	
...	...	Ser X-1	1.6		16	
...	...	XTE J1855−026	2	1.4	7.4	
4	305	GRS 1915+105	26	5.2	476	χ
...	...	Aql X-1[b]	15	6.6	152	
...	...	H 1907+097[a]	3.1		57	
...	...	4U 1909+07	1.5	0.54	24	
...	...	IGR J19140+0951	1.3	0.48	23	
...	...	Ser X-1	1.7		18	
...	...	SS 433	0.7		10	
5	315	GRS 1915+105	22	5.5	297	μ, β
...	...	4U 1909+07[a]	3		39	
...	...	IGR J19140+0951	2.2	0.8	30	
...	...	H 1907+097	2	0.7	26	
...	...	Ser X-1	1.5		11	
...	...	Ginga 1843+009	2.2		12	
...	...	XTE J1855-026	1.7		7.6	
...	...	Aql X-1[b]	0.8 1	6.1		
6	356[c]	GRS 1915+105	6.9	1.9	38	No JEM-X data
...	...	H 1907+097	1.3		7	
...	...	Ser X-1	2.3		7	
...	...	IGR J19140+0951	1.1		6.1	
...	...	4U 1909+07	1.3		6.1	
7	361	GRS 1915+105	15	3.5	268	ϕ, θ, δ
...	...	H 1907+097[a]	3.2		57	
...	...	IGR J19140+0951	2.4	0.8	43	
...	...	4U 1909+07	2.1	0.6	35	
...	...	Ser X-1	1.1		11	
...	...	SS 433	0.6		9.0	
...	...	XTE J1855-026	1.7		7.5	
8	367[d]	GRS 1915+105	22	4.7	242	χ
...	...	H 1907+097[a]	1.3		14	
...	...	4U 1909+07	1.3		13	
...	...	Ser X-1	1.6		10	
9	368[d]	GRS 1915+105	27	5.5	420	χ
...	...	4U 1909+07	1.2	0.6	17	
...	...	H 1907+097[a]	0.9		13	
...	...	SS 433	0.7		8.5	

TABLE 3—*Continued*

Obs. #	Rev. #	Source	Flux (cts/s) 20-40 keV	40-80 keV	20-40 keV significance (σ)	classes
...	...	Ser X-1	1.0		9.0	
...	...	XTE J1855-026	1.5		6.1	
10	373	GRS 1915+105	12	3.1	227	χ, μ, β
...	...	H 1907+097[a]	1.3		23	
...	...	Ser X-1	1.4		13	
...	...	4U 1909+07	0.7		13	
...	...	SS 433	0.6		9.8	
...	...	IGR J19140+0951	0.43		7.7	
11	379	GRS 1915+105	26	6.5	379	δ,μ,β
...	...	Aql X-1[e]	7.1	3.5	60	
...	...	IGR J19140+0951	1.7	0.5	24	
...	...	H 1907+097[a]	0.9		12	
...	...	4U 1909+07	0.95		13	
...	...	Ser X-1	1.2		8.7	
...	...	XTE J1855-026	1.9		8.1	

[a]Detailed analysis of H 1907+097 (a.k.a. 4U 1907+09) during these observations is presented in Fritz et al. (2006)

[b]Analysis of Aql X-1 during these observations is reported in Rodriguez et al. (2006)

[c]Strong solar flares

[d]These two observations were part of a huge multiwavelength campaign on GRS 1915+105 (Ueda et al. 2006)

[e]Rodriguez & Shaw (2005)

FIG. 1.— **Top:** Light curves of GRS 1915+105 from MJD 53 200 to MJD 53 900 as seen a) between 1.2 and 12 keV with the *RXTE*/ASM, and b) at 15 GHz with the RT. In each panel the vertical arrows show the dates of the *INTEGRAL* observations, and the longer arrows show the four particular observations whose accretion ejection properties are discussed in detail in this paper.

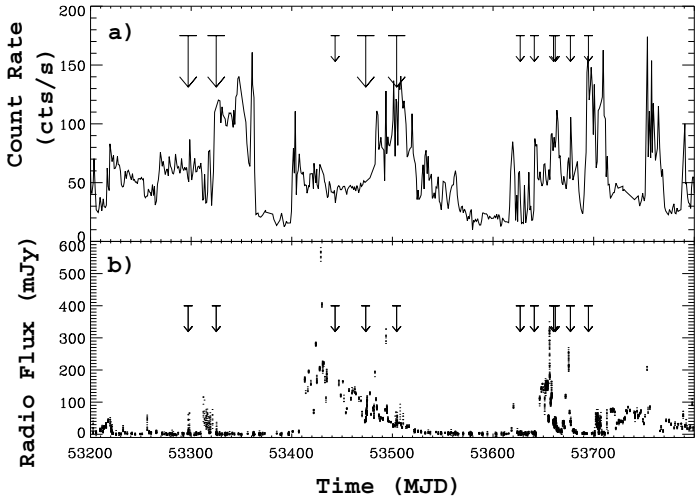

FIG. 2.— **Left:** Light curves of GRS 1915+105 during Obs. 1: a) RT at 15 GHz, b) JEM-X 3–13 keV binned at 20 s, c) ISGRI 18–50 keV binned at 50 s, d) *RXTE*/PCA 2–18 keV binned at 16 s. **Right:** CC diagrams (upper panels) and *RXTE* light curves (lower panels) of 2 sub-intervals from Obs. 1, showing occurrences of class ρ (left) and class ν (right).

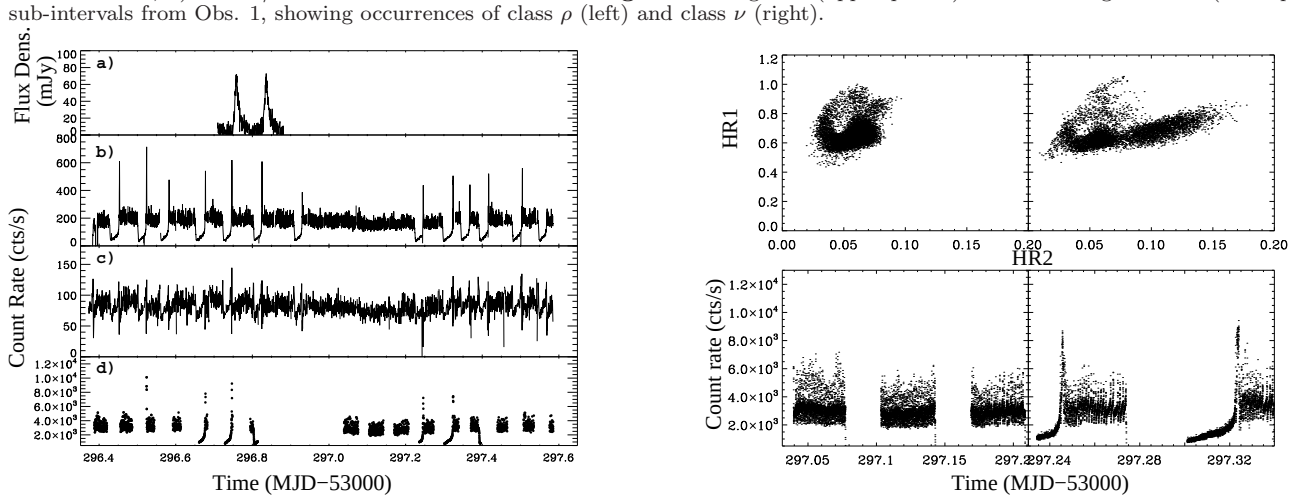

FIG. 3.— **Left:** Same as Fig. 2 for Obs. 2. **Right:** CC diagrams (upper panels) and *RXTE* light curves (lower panels) of 3 sub-intervals from Obs. 2, showing occurrences of class μ/κ (left), class λ (middle) and class γ (right).

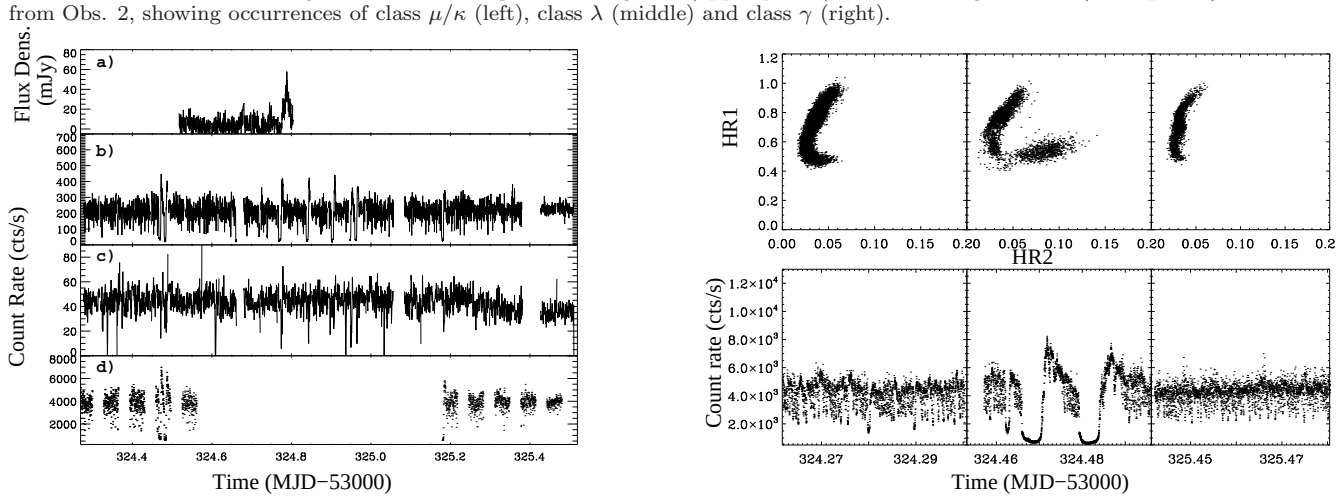

FIG. 4.— Zoom on a portion of Obs. 2 showing in the top panel three radio flares (indicated by the arrows). The other panels show, from top to bottom, the JEM-X 3–13 keV count rate, the ISGRI 18–50 keV count rate, and the 3–13 keV/18–50 keV SR. The box delimited with dashes shows the short cycle preceding the second radio flare.

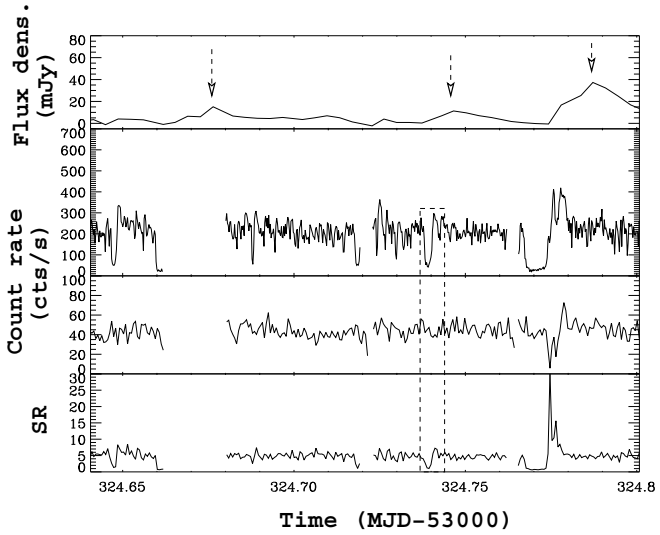

FIG. 5.— **Left:** Light curves of GRS 1915+105 during Obs. 4: a) RT at 15 GHz, b) JEM-X 3–13 keV binned at 50 s, c) ISGRI 18–50 keV binned at 200 s, d) *RXTE*/PCA 2–18 keV binned at 16 s. **Right:** CC diagram (upper panel) and *RXTE* light curve (lower panel) of 1 sub-interval from Obs. 4 showing the source was in class χ.

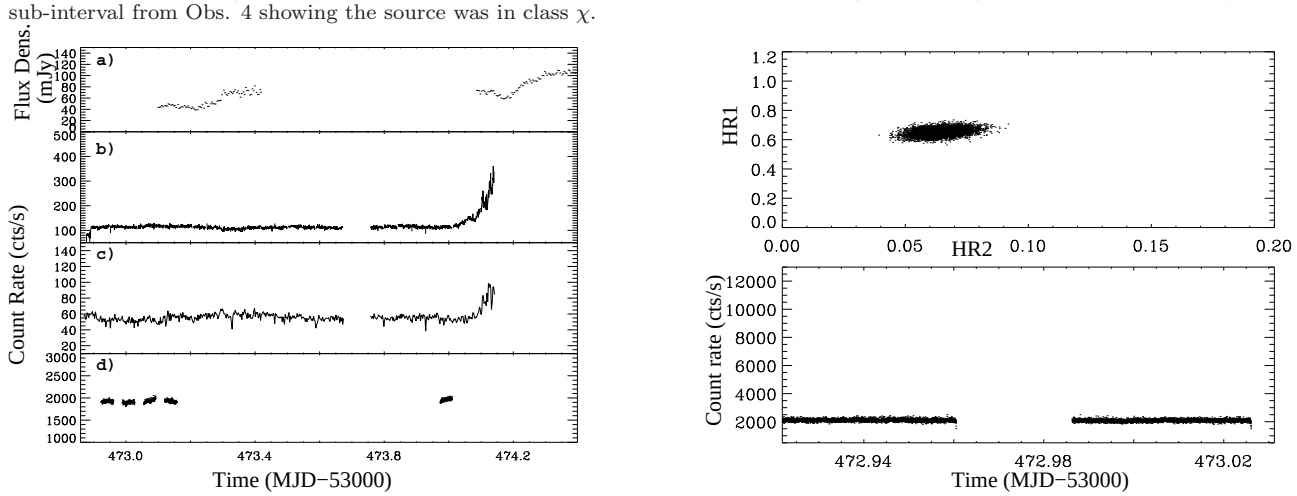

FIG. 6.— **Left:** Same as Fig. 2 for Obs. 5. **Right:** CC diagrams (upper panels) and *RXTE* light curves (lower panels) of 2 sub-interval from Obs. 5 showing occurrences of class μ and β.

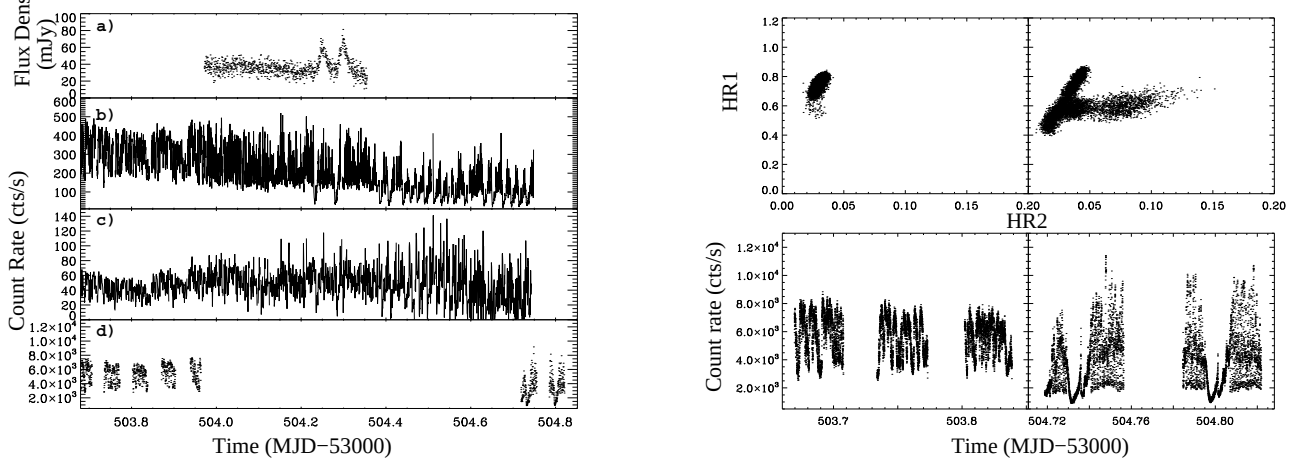

FIG. 7.— Zooms on portions of Obs. 2, 3 and 5 (from left to right). **Top panel:** JEM-X 3–13 keV light curves with for each observations the 3 intervals with specific properties discussed in the text. **Middle panel:** 18–50 keV ISGRI light curves. **Bottom panel**: 3–13 keV/18–50 keV SR. Note that different vertical scales of each individual plots.

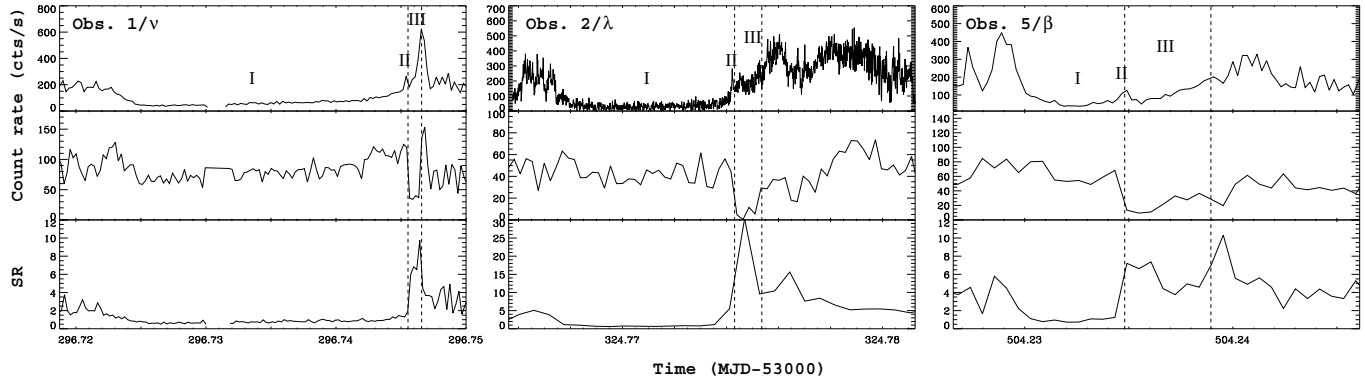

FIG. 8.— Evolution of the amplitude of the radio flares vs. the duration of the preceding X-ray dip. The points are from this study and the triangles come from Pooley & Fender (1997), and Klein-Wolt et al. (2002). The line represents the linear function that best fits the data.

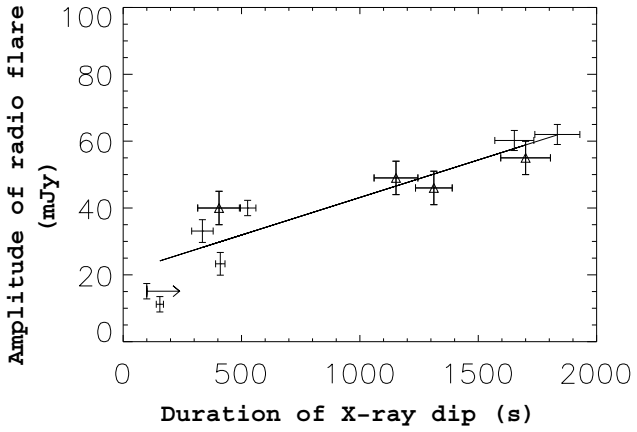

FIG. 9.— **Left:** Light curves of GRS 1915+105 during Obs. 3: a) JEM-X 3–13 keV binned at 50 s, b) ISGRI 18–50 keV binned at 200 s, c) *RXTE*/PCA 2–18 keV binned at 16 s. **Right:** CC diagram (upper panel) and *RXTE* light curve (lower panel) of a sub-interval from Obs. 3 showing the source was in class χ.

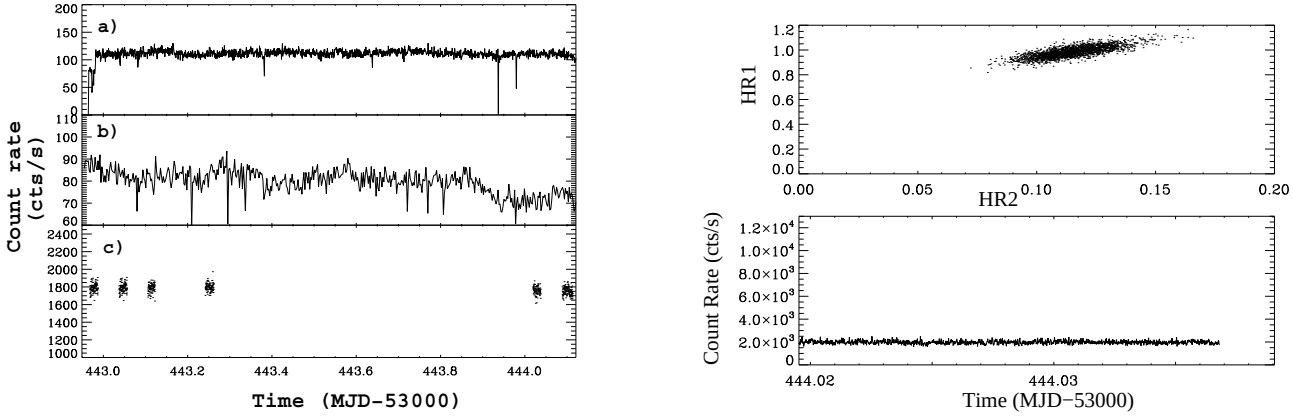

FIG. 10.— **Left:** Light curves of GRS 1915+105 during Obs. 7: a) RT at 15 GHz, b) JEM-X 3–13 keV binned at 20 s, c) ISGRI 18–50 keV, binned at 100 s. **Right:** CC diagrams (upper panels) and *RXTE* light curves (lower panels) of 2 sub-interval from Obs. 7 showing the source was in class ϕ at the beginning and class δ in the end. Note that between those two classes GRS 1915+105 transited through a class θ.

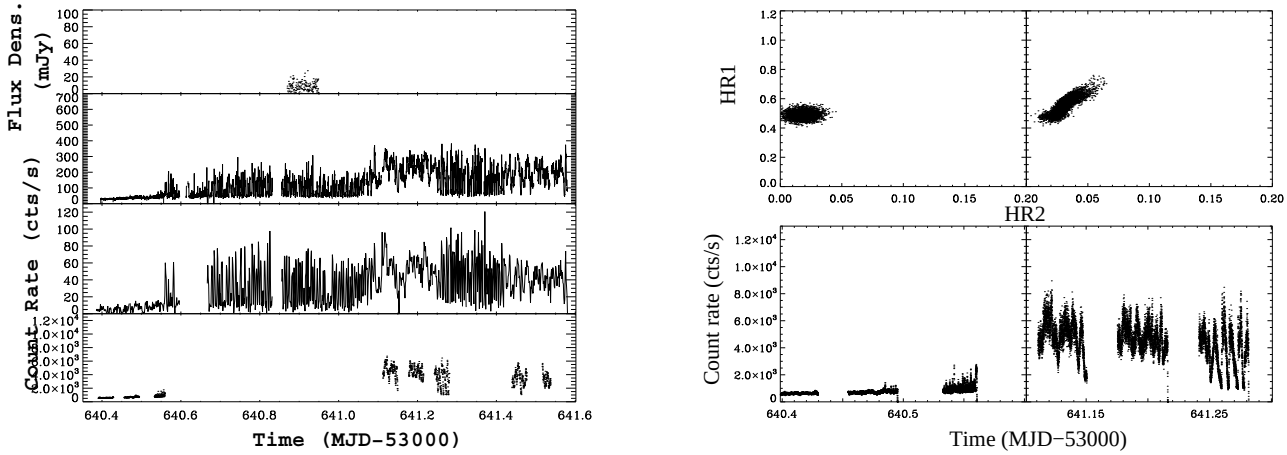

FIG. 11.— Zoom on a sub-interval from Obs. 7. From top to bottom the plots respectively represent the JEM-X 3–13 keV , ISGRI 18–50 keV light curves and the 3–13 keV/18–50 keV SR. Both light curves show "M-shape" patterns typical of class θ.

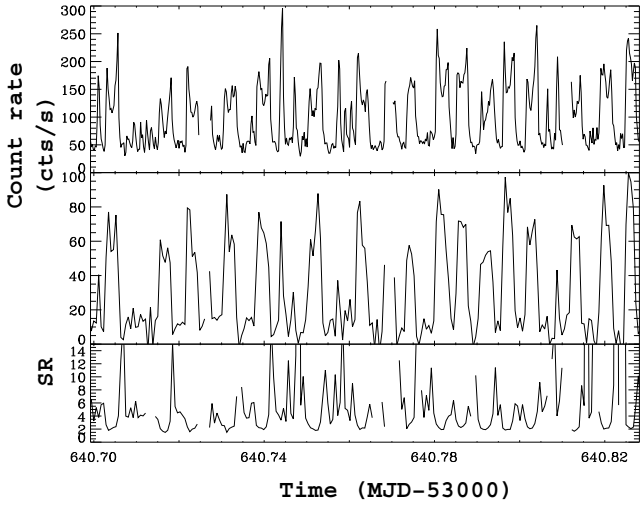

FIG. 12.— **Left:** Light curves of GRS 1915+105 during Obs. 8 and 9: a) RT at 15 GHz, b) JEM-X 3–13 keV binned at 20 s, c) ISGRI 18–50 keV binned at 100 s. The source starts in class χ in the first part, transits to class θ (not visible here, see Ueda et al. 2006) and transits back in a likely class χ in the second interval visible here. **Right:** Zoom on two sub-intervals from Obs. 8 (left panel) and Obs. 9 (right panel). From top to bottom the plots respectively represent the JEM-X 3–13 keV , ISGRI 18–50 keV light curves and the 3–13 keV/18–50 keV SR.

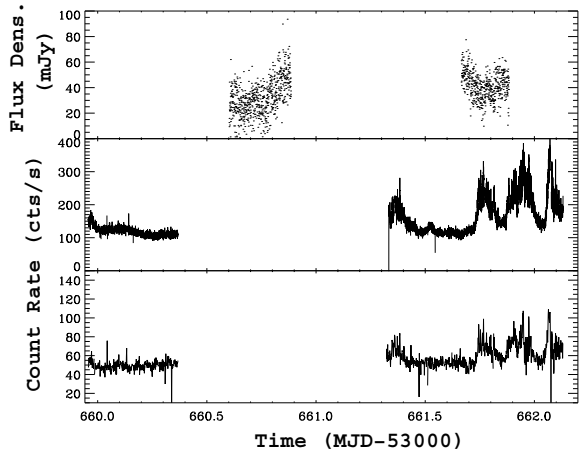

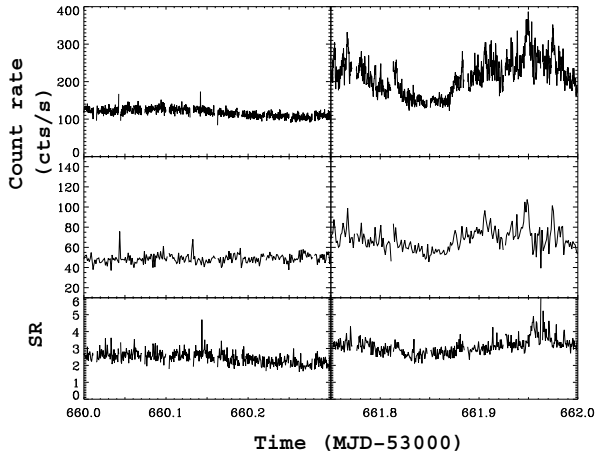

FIG. 13.— **Left:** Light curves of GRS 1915+105 during Obs. 10: a) RT at 15 GHz, b) JEM-X 3–13 keV, c) ISGRI 18–50 keV. **Right:** Zoom on 3 sub intervals of Obs. 10 showing (possible) occurences of class δ, μ, and β. From top to bottom the panels respectively show the JEM-X 3–13 keV, and ISGRI 18–50 keV light curves and the 3–13 keV/18–50 keV SR.

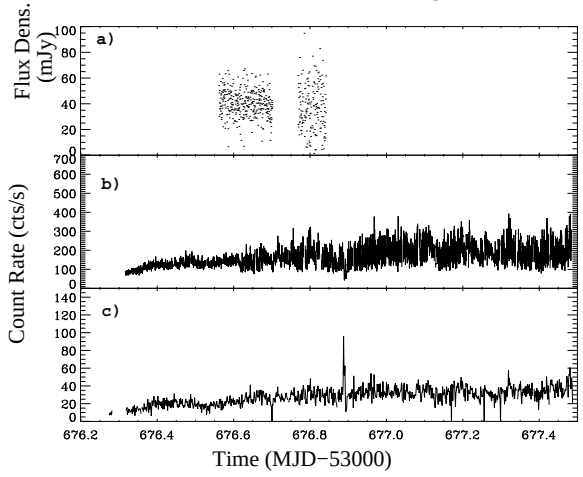

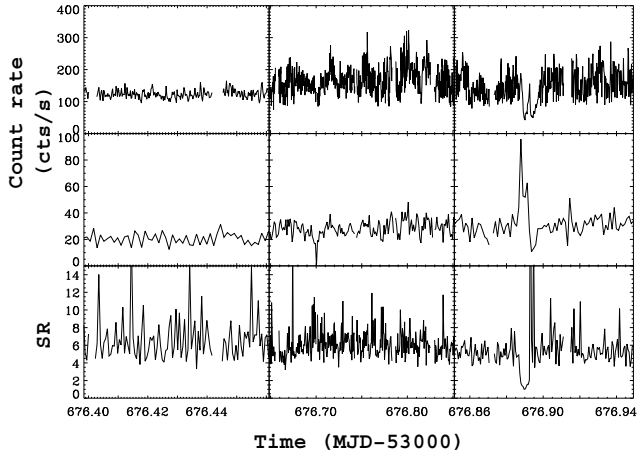

FIG. 14.— **Left:** Light curves of GRS 1915+105 during Obs. 11: a) JEM-X 3–13 keV binned at 20 s, b) ISGRI 18–50 keV binned at 100 s c) PCA 2–18 keV binned at 16 s. **Right:** Zoom on 3 sub intervals showing occurrences of class δ (possibly), μ and β.